







Structural, electronic, and photocatalytic water splitting in two-dimensional monolayer $MNXY$ ($M/N = \text{Al, Ga}$, $X/Y = \text{N, P, As}$) semiconductors: A first-principles perspective

Yutao Liu , Tinghong Gao,^{*} Guolin Qian, Xinzhu Tan , Songli Dai, Yue Gao , Lianxin Li ,
Quan Xie, Qian Chen, and Junjie Wang 

Institute of Advanced Optoelectronic Materials and Technology, College of Big Data and Information Engineering, Guizhou University, Guiyang 550025, China

 (Received 5 September 2023; revised 3 November 2023; accepted 4 December 2023; published 26 December 2023)

The exploration of novel and stable two-dimensional (2D) materials holds considerable significance in the development of optoelectronic devices and photocatalytic water splitting. Herein, $MNXY$ ($M/N = \text{Al, Ga}$, $X/Y = \text{N, P, As}$) monolayers are constructed based on 2D double-layer honeycomb structures. Six stable semiconductor types were screened through first-principles calculations, and their mechanical, electrical, optical, and transport properties as well as their applications in photocatalytic water splitting were investigated. We found that the six stabilized $MNXY$ monolayers had band gaps of 0.846–3.806 eV. The mechanical properties indicate that AlGaN_2 has a Young's modulus exceeding 100 N/m, whereas the remaining five monolayers exhibit values below this threshold. The hole carrier mobility of the AlGaN_2 monolayer along the armchair direction reaches an ultrahigh value of $3649.21 \text{ cm}^2 \text{ V}^{-1} \text{ s}^{-1}$; thus it has the potential for application in optoelectronic devices. Furthermore, we observed that AlGaP_2 monolayers exhibit band-edge potentials spanning the redox potential of water, a considerable difference in electron-hole carrier mobility, strong visible light absorption, and a high solar to hydrogen efficiency (17.51%) in the absence of strain, making them suitable for photocatalytic water splitting. We expect that our results will pave the way forward for material selection for next-generation optoelectronic devices and photocatalysts.

DOI: [10.1103/PhysRevB.108.245424](https://doi.org/10.1103/PhysRevB.108.245424)

I. INTRODUCTION

Two-dimensional (2D) materials constitute an immensely diverse group that encompasses several classes, such as graphene [1], black phosphorus [2], transition metal dichalcogenides [3], and gallium nitride (GaN) [4]. These materials have very thin structures because they comprise only a single layer or a few layers of atoms, giving them an advantage in application in micro- and nanoscale devices. The resulting wide range of applications includes the manufacture of high-mobility transistors [5], flexible electronics [6], high-performance integrated circuits [7], efficient catalysts [8], and solar cells [9]. Several attempts have been made to search for new types of 2D materials to explore the potential for new physical phenomena and applications, thus driving the frontiers in the field of 2D materials. Typically, 2D materials are derived from van der Waals-layered materials, where the bonding between layers can be easily broken due to the weakening of van der Waals interactions. Thus the corresponding 2D materials can be prepared via physical or chemical stripping [10,11]. The research and development of 2D materials can help achieve advancements in the field of materials science while providing compelling opportunities for the design and application of novel materials.

In 2018, Lucking *et al.* theorized a 2D material with a two-layer hexagonal-like structure and named it a double-layer

honeycomb (DLHC) structure [12]. Its formation energy was theoretically calculated and confirmed to be lower than that of truncated bulk and other 2D materials, such as AlSb [13,14], CdTe [15], and InAs [16]. After extensive study, this class of 2D materials was experimentally successfully prepared [17,18]. Theoretical studies have shown that the configuration of DLHCs from conventional three-dimensional (3D) semiconductors, such as the III-V, II-VI, and I-VII families, is stable, thus possessing a new group of 2D material families [12]. Notably, few other structures have been previously realized as stable 2D materials of the I-VII family. Thus the emergence of DLHC structures has broadened the scope of 2D materials, attracting numerous scholars to study their novel physicochemical properties.

Precisely substituting atoms in semiconductors is crucial for semiconductor devices and electronics. This enables adjusting its electronic energy level structure, carrier concentration, and band structure, thereby altering electrical conductivity, photovoltaic properties, and magnetic properties [19–22]. This modification method helps to improve the performance of semiconductor devices (e.g., transistors and photodiodes) and enables the creation of semiconductor materials with specific properties, such as solar cells, to optimize photovoltaic conversion efficiencies and optical communication devices for achieving high-speed signal transmission. MoSH was experimentally prepared by replacing S atoms on one side with H. The transformation of MoS_2 semiconductors into metallic MoSH has been realized, which has a very high intrinsic carrier concentration ($\sim 2 \times 10^{13} \text{ cm}^{-2}$) [23].

^{*}gaotinghong@sina.com

Inspired by the successful preparation of Ga_2S_3 with five atomic layer structures [24,25], Hieu *et al.* formed a Janus structure by replacing one S atom of the protocell with $X = \text{O}, \text{S}, \text{Se}$ through first-principles calculations and thoroughly investigated the electronic, mechanical, and carrier mobility of the replacement structure [26]. Similarly, Qi *et al.* replaced the atoms of this Janus structure with Al_2XYZ ($X/Y/Z = \text{S}, \text{Se}, \text{Te}, X \neq Y \neq Z$) and found that Al_2XYZ is highly efficient in the photocatalytic decomposition of water and Al_2SeTeS has good piezoelectric properties [27]. Liu *et al.* constructed a monolayer $\text{Sn}_2\text{S}_2\text{P}_4$ structure based on 2D SnP_3 [28], which possesses an indirect band gap of 1.77 eV and well spans the redox potential of water; the hydrogen production efficiency is as high as 17.51%, making it a highly efficient photocatalyst [29]. Lu *et al.* prepared Janus MoSSe by controlled vulcanization of a monolayer of MoSe_2 by replacing the upper layer of Se atoms with S atoms while the lower layer remained unchanged [23]. Subsequently, the researchers found that the 2D MXY ($M = \text{Mo}, \text{W}; X, Y = \text{S}, \text{Se}, \text{Te}$) is an efficient catalyst due to the built-in electric field through first-principles calculations [30].

Herein, we constructed 2D MNXY ($M, N = \text{Al}, \text{Ga}, X, Y = \text{N}, \text{P}, \text{As}$) monolayers based on DLHC structures and screened six stable semiconductors using first-principles calculations. We also investigated the mechanical, electrical, intrinsic carrier mobility, optical properties, and applications of photocatalytic water splitting. Our results provide theoretical guidance for broadening the family of DLHC structures. Moreover, these results represent an important advance in our understanding of the structural features of these honeycombs. We expect our findings will point the way forward for these structures in optoelectronic devices and efficient photocatalysts.

II. CALCULATION METHOD

All calculations in this paper were carried out using the projector augmented wave (PAW) method based on density functional theory (DFT) with a plane wave basis set. The computations are executed using the Vienna *ab initio* simulation software [31,32]. The generalized gradient approximation according to the Perdew-Burke-Ernzerhof (PBE) scheme is chosen for geometric structure optimization, while the Heyd-Scuseria-Ernzerhof (HSE06) functional with mixing parameters $\alpha = 0.25$ is employed to acquire more precise electronic band structures [33–35]. A cutoff energy of 450 eV and a vacuum region with a thickness of 20 Å are employed to avoid cyclic interactions in the C direction, and a k mesh of $\Gamma 11 \times 11 \times 1$ and $21 \times 21 \times 1$ is applied for Brillouin-zone integration in the structure optimization and electronic structure calculation, respectively. The convergence values for energy and force are set at 10^{-6} eV and 0.01 eV/Å, respectively. The dipole moment correction is applied to all structures [36]. To achieve more accurate calculations of optical properties, the dielectric constant was computed using the HSE06 functional based on the independent-electron approximation, thereby obtaining the optical absorption coefficient. Phonon spectra are derived through the implementation of density functional perturbation theory (DFPT) within the PHONOPY code [37,38] using a $4 \times 4 \times 1$ k mesh and $4 \times 4 \times 1$

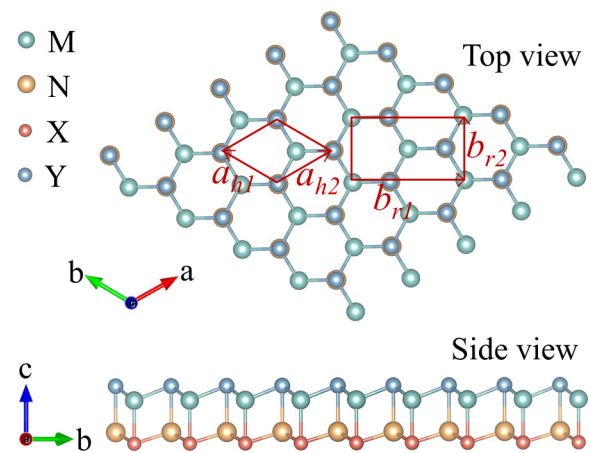


FIG. 1. Top and side views of MNXY ($M, N = \text{Al}, \text{Ga}, X, Y = \text{N}, \text{P}, \text{As}$). The diamond and rectangular boxes represent the unit cell and supercell, respectively.

supercell containing 64 atoms. *Ab initio* molecular dynamics (AIMD) simulation was performed using a $4 \times 4 \times 1$ supercell at 300 K under the NVT ensemble with the temperature controlled by the Nosé-Hoover method; a time step of 2 fs was employed for a duration of 8 ps to assess the structural thermal stability.

III. RESULTS AND DISCUSSIONS

A. Geometric properties and stability

The atomic structures of MNXY ($M/N = \text{Al}, \text{Ga}/X, Y = \text{N}, \text{P}, \text{As}$) are shown in Fig. 1. The structure consists of a bilayer hexagonal arrangement, and the side view presents it in a zigzag shape. When M equals N and X equals Y , MNXY can be abbreviated as MX . However, since Faraji *et al.* have already discussed the specific electronic properties of MX [39], this study will not delve into it further, resulting in 15 distinct structural forms. The structural models obtained after conducting structural optimization using different atomic substitutions are illustrated in Fig. S1 in the Supplemental Material [40]. We found that the side containing N atoms tended to form a planar shape, whereas the side containing P and As atoms tended to form a zigzag shape. The unit cell of the MNXY monolayers contains four atoms, and its lattice constant varies from 3.245 to 4.03 Å. The lattice constant of MNXY increases as the element radius increases. All computed lattice constants are presented in Table I.

The main aim of this study is to investigate the semiconductor properties of monolayer MNXY . Initially, we conducted band structure calculations for all structures using the PBE functional. The resulting band structures are shown in Fig. S2 in the Supplemental Material [40]. A more detailed analysis of the electronic structure is elaborated upon in the following sections. As a preliminary screening, we observed that seven structures, such as Al_2NAs , exhibited metallic properties. These structures will not be considered further in subsequent analyses. Notably, while the PBE functional tended to underestimate band gaps, some structures obtained might fall into the semiconductor category, but the resulting band gaps could

TABLE I. Lattice constant a , band gap E_g under PBE and HSE06 functional, type, phonon spectra without imaginary frequency, and the structure to remain stable during an 8 ps relaxation at 300 K is labeled as stable; otherwise, it is considered unstable. Cohesive energy E_{coh} , work function W_f .

Structure	a (Å)	E_g (eV)/PBE	E_g (eV)/HSE06	Type	Phonon dispersion spectra	AIMD	E_{coh} (eV/atom)	W_f (eV)
Al ₂ NAs	3.581	—	—	Metallic	—	—	—	—
Al ₂ NP	3.567	0.786	1.529	Direct	Stable	Unstable	—	—
Al ₂ PAs	3.982	1.301	1.972	Indirect	Stable	Stable	4.697	5.295
Ga ₂ NAs	3.597	—	—	Metallic	—	—	—	—
Ga ₂ NP	3.579	—	—	Metallic	—	—	—	—
Ga ₂ PAs	3.971	—	—	Metallic	—	—	—	—
AlGaNP	3.245	2.560	3.806	Indirect	Stable	Stable	6.403	5.395
AlGaP ₂	3.911	1.048	1.884	Direct	Stable	Stable	4.566	5.549
AlGaAs ₂	4.030	0.181	0.895	Direct	Stable	Stable	4.158	5.003
AlGaNAs	3.619	—	—	Metallic	—	—	—	—
AlGaNP	3.650	0.188	0.846	Direct	Stable	Unstable	—	—
AlGaPAs	3.972	0.351	1.132	Direct	Stable	Stable	4.342	5.195
GaAlNAs	3.551	—	—	Metallic	—	—	—	—
GaAlNP	3.533	—	—	Metallic	—	—	—	—
GaAlPAs	3.966	0.543	1.287	Direct	Stable	Stable	4.371	4.964

be too small for practical semiconductor device applications [41].

Further, we computed the phonon spectra of the $MNXY$ monolayers to assess their dynamic stability as shown in Fig. 2. If their phonon spectra has no imaginary frequency, the structure is dynamically stable. Owing to the presence of four atoms in the $MNXY$ unit cell, the phonon spectra comprises 12 vibrational branches. Longitudinal acoustic, transverse acoustic,

and zigzag acoustic modes occur only at low frequencies, whereas optical modes occur at high frequencies [42]. For AlGaPAs monolayers [Fig. 2(g)], there is almost no gap between the optical and acoustic branches, which can result in considerable photoacoustic scattering [26]. The $MNXY$ monolayers exhibit crystal symmetry within the C_{3v} group. At the Γ point, the vibrational modes of $MNXY$ undergo decomposition into $C_{3v} = 4A_1 \oplus 4E$. Within the optical phonon modes, the

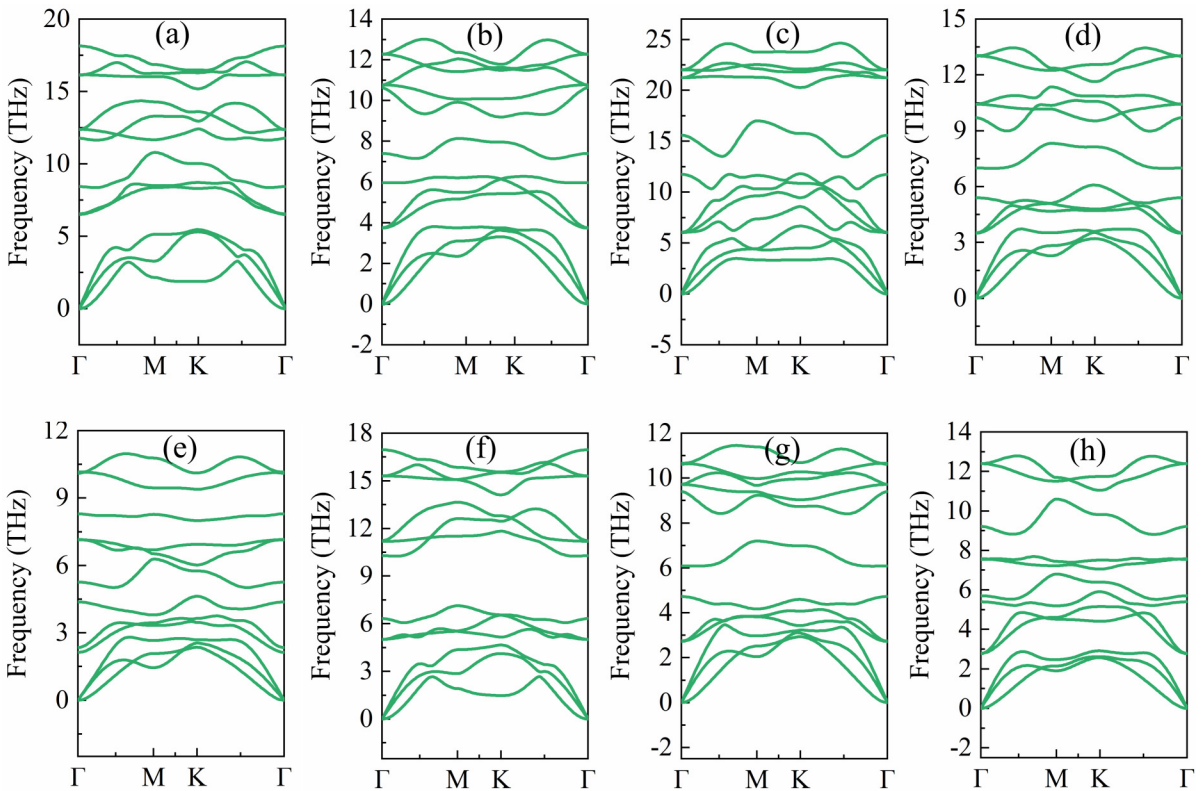


FIG. 2. The phonon spectra of the $MNXY$ monolayers. (a) Al₂NP, (b) Al₂PAs, (c) AlGaNP, (d) AlGaP₂, (e) AlGaAs₂, (f) AlGaNP, (g) AlGaPAs, (h) GaAlPAs.

TABLE II. The elastic constants, Young's modulus, and Poisson's ratio values of the six monolayers.

Structure	C_{11}/C_{22} (N/m)	C_{12}/C_{21} (N/m)	C_{66} (N/m)	Young's modulus (N/m)	Poisson's ratio
Al ₂ PAs	86.259	27.467	29.396	77.513	0.318
AlGaNP ₂	193.538	67.653	62.942	169.889	0.350
AlGaP ₂	91.311	24.458	33.427	84.760	0.268
AlGaAs ₂	80.916	22.393	29.262	74.719	0.277
AlGaPAs	84.292	23.077	30.608	77.975	0.274
GaAlPAs	89.464	25.799	31.833	82.024	0.288

nondegenerate and doubly degenerate phonon modes manifest at the high-symmetry point. The nondegenerate and doubly degenerate phonon modes correspond to the A_1 vibrational and E modes, respectively. The A_1 vibrational modes encompass the nondegenerate phonon modes, whereas the doubly degenerate phonon modes align with the E modes. In particular, the nondegenerate phonon modes denoted as A_1 correspond to the out of plane optical (ZO) modes. Moreover, the doubly degenerate phonon mode occurring at the Γ point arises as a blend of the in-plane transverse optical (TO) and in-plane longitudinal optical (LO) modes. Sohler *et al.* also presented an approach to rectifying the LO-TO splitting in 2D structures using the DFPT method [43]. The lack of imaginary frequency in the phonon spectra confirms the dynamic stability of the structures of the eight monolayer semiconductors.

To validate the thermodynamic stability of the eight structures, we employed AIMD to run simulations at 300 K under NVT ensembles using the Nosé-Hoover thermostat method for 8 ps (4×4 supercell) to evaluate their stability. The results are depicted in Fig. S3 in the Supplemental Material [40]. We observed energy drops at around 4 and 2 ps for the Al₂NP [Fig. S3(a)] and AlGaNP [Fig. S3(f)] monolayers, respectively, accompanied by notable structural distortion and bond breaking (see Fig. S4 in the Supplemental Material [40]), indicating the thermodynamic instability of these two structures. The temperature and energy profiles of the remaining six structures maintain regular oscillations and gradually decrease in amplitude, and the structures do not undergo considerable deformation or phase transition. Hence, for 2D materials, relying solely on phonon spectra to determine the structural stability of materials in previous research is insufficient. Thus we identified six monolayer structures that meet the dynamic and thermodynamic stability criteria.

Cohesive energy serves as an indicator to determine whether a structure is energetically favorable. Its expression is given by [44]

$$E_{\text{coh}} = \frac{N_M E_M + N_N E_N + N_X E_X + N_Y E_Y - E_{MNXY}}{N_M + N_N + N_X + N_Y}. \quad (1)$$

Here, N represents the number of atoms for the respective element, and E represents the energy. The calculated cohesive energies for the six structures are presented in Table I. It can be observed that the cohesive energy values have a range of 4.158–6.403 eV. The cohesive energies of the six monolayer structures maintain energy stability. Moreover, AlGaNP₂ (6.403 eV/atom) exhibits a relatively more energetically favorable behavior than 2D Janus Ga₂SX₂ (3.77–5.24 eV/atom) [26], phosphorene (3.30 eV/atom) [45],

Sn₂S₂P₄ (4.72 eV/atom) [29], and silicene (3.91 eV/atom) [46].

B. Mechanical properties

The mechanical properties of materials are crucial parameters to consider in device applications. For 2D materials, the elastic constants and moduli were acquired through Hooke's law, considering the plane-stress conditions [47],

$$\begin{bmatrix} \sigma_{xx} \\ \sigma_{yy} \\ \sigma_{xy} \end{bmatrix} = \begin{bmatrix} C_{11} & C_{12} & 0 \\ C_{21} & C_{22} & 0 \\ 0 & 0 & C_{66} \end{bmatrix} \begin{bmatrix} \varepsilon_{xx} \\ \varepsilon_{yy} \\ 2\varepsilon_{xy} \end{bmatrix}, \quad (2)$$

where C_{11} , C_{12} , C_{21} , C_{22} , and C_{66} represent the elastic stiffness constants. The calculated elastic stiffness constants for the six structures are presented in Table II. All structures fulfill the Born-Huang stability criteria: $C_{11} > |C_{12}|$, $C_{11}C_{22} - C_{12}^2 > 0$, $C_{66} > 0$, indicating the mechanical stability of these six structures. With the elastic stiffness, we can calculate the Young's modulus and Poisson's ratio using the following expressions [48]:

$$Y(\theta) = \frac{C_{11}C_{22} - C_{12}^2}{C_{11}\sin^4\theta + P\sin^2\theta\cos^2\theta + C_{22}\cos^4\theta}, \quad (3)$$

$$\nu(\theta) = \frac{C_{12}\sin^4\theta - Q\sin^2\theta\cos^2\theta + C_{12}\cos^4\theta}{C_{11}\sin^4\theta + P\sin^2\theta\cos^2\theta + C_{22}\cos^4\theta}, \quad (4)$$

where $P = (C_{11}C_{22} - C_{12}^2)/C_{66} - 2C_{12}$ and $Q = C_{11} + C_{22} - (C_{11}C_{22} - C_{12}^2)/C_{66}$; θ is the angle within the plane. The specific values of the calculated Young's modulus and Poisson's ratio are also presented in Table II. Among these, AlGaAs₂ (74.719 N/m) and AlGaNP₂ (169.889 N/m) exhibit the smallest and largest Young's modulus, respectively, whereas AlGaP₂ (0.268) and AlGaNP₂ (0.35) display the smallest and largest Poisson's ratios, respectively. Notably, the calculated Young's modulus for the six structures are lower than those widely studied 2D materials, such as graphene (342.2 N/m) [49], *h*-BN (275.8 N/m) [50], and MoS₂ (130 N/m) [51]. This reduced Young's modulus suggests its applicability to various strains. The Young's moduli as polar plots against different directions are shown in Fig. 3. It is evident that the mechanical behavior exhibits isotropic characteristics. The exceptional mechanical properties indicate that stable *MNXY* monolayers have potential applications in flexible electronics. Owing to the structural similarity, we only take the Al₂PAs monolayer as an example (see Fig. S5 of the Supplemental Material [40]). Monolayer Al₂PAs can achieve an ultrahigh strain of 23% under biaxial tensile strain and up to 14% under compressive strain.

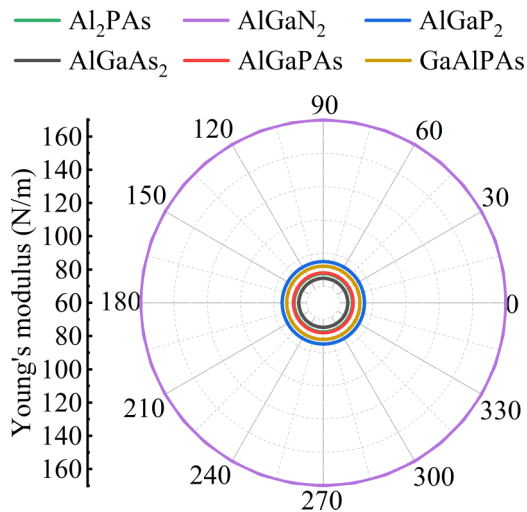


FIG. 3. Polar plots of Young's modulus $Y(\theta)$ of six monolayers.

C. Electronic properties

We investigate the electronic structural properties of the six stable $MNXY$ monolayers. To unveil the bonding information among the four categories of atoms M , N , X , and Y , we

constructed the electron local functions (ELFs) as shown in Fig. S6 of the Supplemental Material [40]. ELF is a tool often employed to study electronic structures. When $ELF = 1$, it indicates complete electron localization; $ELF = 1/2$ represents the paired probability for the corresponding electronic-gas-like behavior; and $ELF = 0$ corresponds to complete electron delocalization, indicating the absence of electrons [52]. The deep purple regions are predominantly situated around the X and Y atoms, whereas the red regions are primarily located near the M and N atoms. We find that the primary chemical bonding in the $MNXY$ monolayer is ionic.

Figure 4 shows the band structures of the six $MNXY$ monolayers under the PBE and HSE06 functionals. The variations in the curves are nearly identical under both functionals, and the positions of the high-symmetry points remain consistent. The HSE06 functional yields larger band gaps. Notably, Al_2PAs and $AlGaN_2$ function as indirect band gap semiconductor materials. In particular, Al_2PAs has its valence band maximum (VBM) located at the high-symmetry point Γ , whereas the CBM is at point M . Meanwhile, for $AlGaN_2$, the conduction band minimum (CBM) occurs at point Γ , and the VBM lies between points K and Γ . The remaining four structures exhibit the characteristics of direct band gap semiconductors, with the CBM and VBM located at point Γ . It

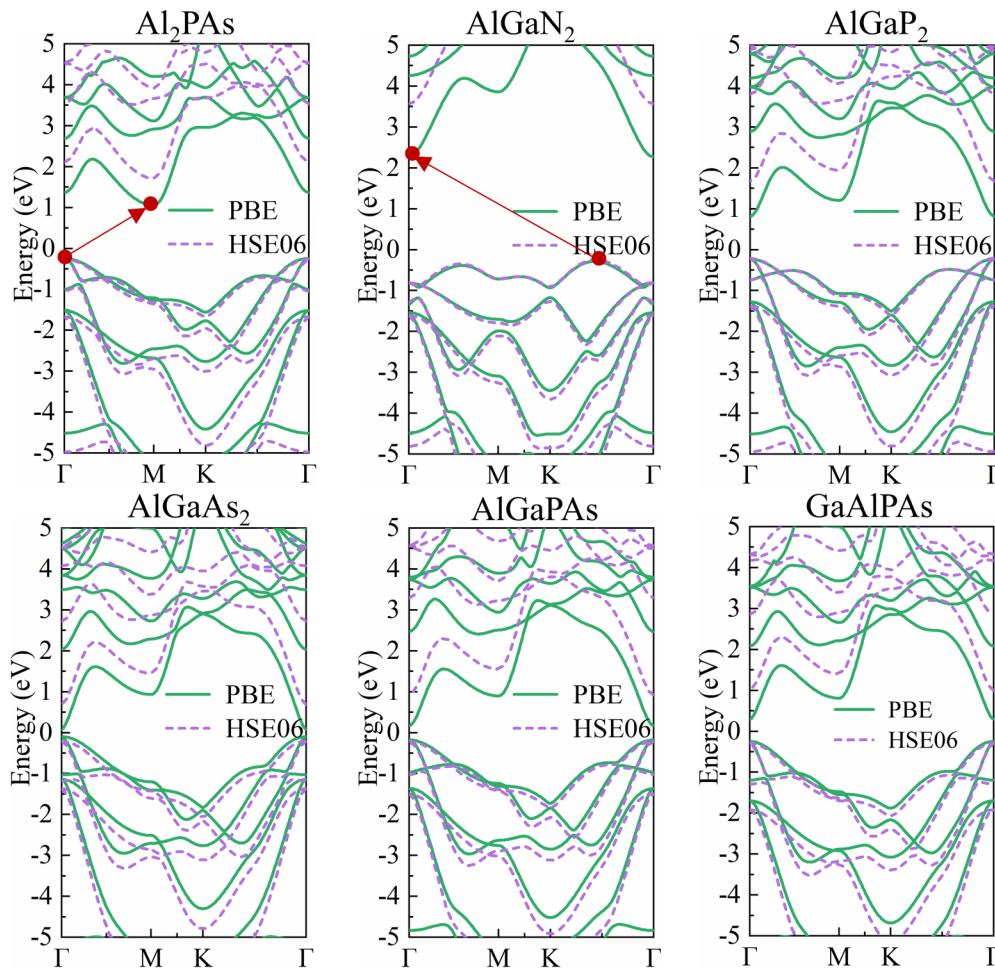


FIG. 4. Band structures of the six monolayers. The solid green and dotted purple lines represent the results obtained using the PBE and HSE06 functionals, respectively.

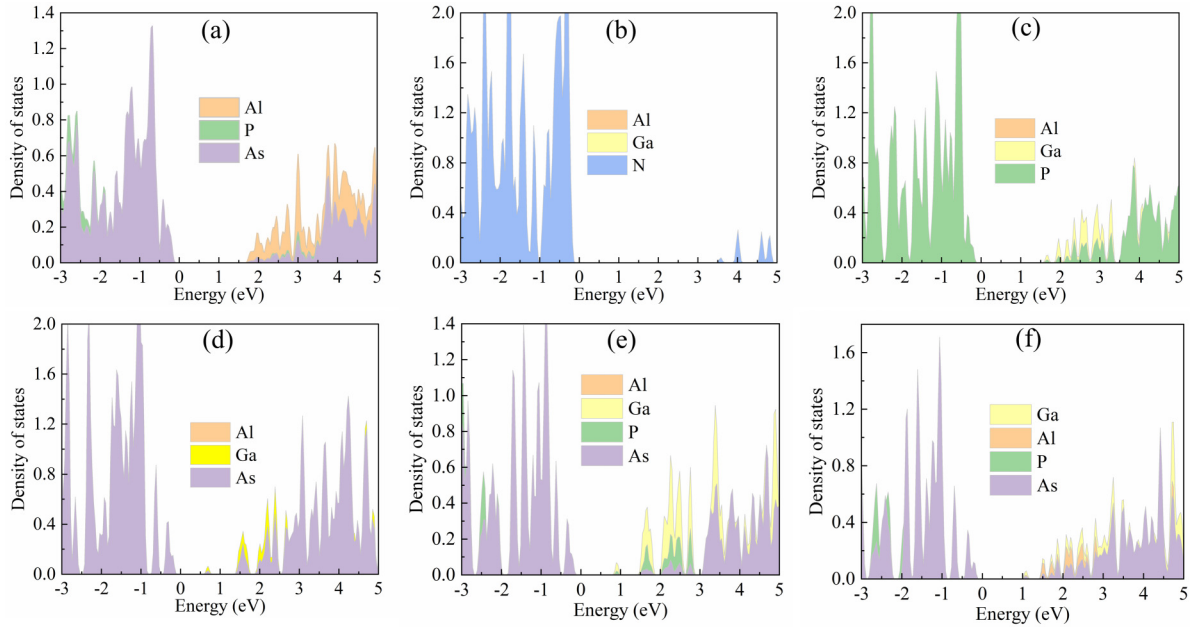


FIG. 5. Density of states of the six monolayers. (a) Al₂PAs, (b) AlGaN₂, (c) AlGaP₂, (d) AlGaAs₂, (e) AlGaPAs, (f) GaAlPAs.

is noteworthy that the minimum values of the conduction band at points Γ and M for Al₂PAs and AlGaP₂ are relatively close. Similarly, for AlGaN₂, the energy difference between points Γ and M and VBM is also slight. Thus these structures might undergo changes in the CBM and VBM under minor external stress or electric fields, potentially influencing the semiconductor type. Under the PBE functional, the band gap values of the eight semiconductor materials fluctuate between 0.181 and 2.56 eV (0.846–3.806 eV under the HSE06 functional). The work function range under the HSE06 functional is 4.964–5.549 eV, as illustrated in Table I. These band gap values, comparable to those of well-established semiconductors, such as silicon (1.1 eV) [53] and GaN (3.4 eV) [54], indicate considerable potential for the application of the MNXY monolayer in electronic devices. Direct band gap semiconductors are more suitable for light-emitting applications because of their efficient photon emission, whereas indirect band gap semiconductors are commonly used in electronic applications where charge carrier mobility and conductivity are crucial [55].

Figure 5 shows the projected density of states for the six MNXY monolayers. It can be observed that except for AlGaN₂ [Fig. 5(b)], the valence bands of the other five structures are primarily contributed by the Y element (considered Y element if $X = Y$), whereas the conduction bands are predominantly influenced by M (or N) elements, with their contribution being greater than that of the X (or Y) elements. For AlGaN₂, the conduction and valence bands are mainly influenced by the N element.

D. Intrinsic carrier mobilities

The intrinsic carrier mobility of a semiconductor is a crucial metric for assessing electron and hole mobility within the material. Computing intrinsic carrier mobility primarily relies on the theory of deformation potential developed by Bardeen and Shockley. We developed a rectangular supercell based on the primitive cell, with the b_1 direction labeled as the

armchair and the b_2 direction labeled as the zigzag direction, as depicted in Fig. 1. The calculation of intrinsic carrier mobility is given as follows [56]:

$$\mu = \frac{e\hbar^3 C_{2D}}{k_B T m^* \bar{m} E_d^2}, \quad (5)$$

where e represents the elementary charge, \hbar is the reduced Planck constant, C_{2D} denotes the elastic constant, k_B is the Boltzmann constant, T is the temperature at 300 K, m^* represents the effective mass, \bar{m} represents the average effective mass in the armchair and zigzag directions, and E_d represents the strain potential energy. It is worth noting that C_{2D} , m^* , and E_d are the values for calculating directionality and are not orientationally averaged. The effective mass represents the proportionality coefficient between electrons or holes and acceleration when subjected to external forces. It is obtained by fitting a quadratic function to the CBM and VBM after applying strain. The specific formula is given as follows:

$$m^* = \frac{\hbar^2}{\frac{\partial^2 E(k)}{\partial k^2}}. \quad (6)$$

The C_{2D} , E_d , m^* , and intrinsic carrier mobility μ values for the six structural calculations are presented in Table III. Apart from AlGaN₂, the electron mobility of the other five structural configurations is consistently higher than the hole mobility in the armchair and zigzag directions. For instance, in the case of AlGaP₂, the electron mobility is approximately 4.4 times that of the hole mobility in the armchair direction, while in the case of GaAlPAs, the electron mobility is roughly 3.2 times that of the hole mobility in the zigzag direction. Along the armchair direction, the hole mobility of AlGaN₂ reaches 3649.21 cm²V⁻¹s⁻¹, surpassing the electron mobility of 1055.54 cm²V⁻¹s⁻¹. Similarly, in the zigzag direction, the hole mobility reaches 2898.91 cm²V⁻¹s⁻¹, surpassing the electron mobility of 903.598 cm²V⁻¹s⁻¹. This disparity arises because the deformation potential energy for holes in

TABLE III. The values of C_{2D} (elastic constant), E_d (deformation potential constant), m^* (carrier effective masses), and μ (carrier mobilities) of the six structures.

Structure	Direction	C_{2D} (J m ⁻²)	E_d (eV)		m^* (m ₀)		μ (cm ² V ⁻¹ s ⁻¹)	
			Electron	Hole	Electron	Hole	Electron	Hole
Al ₂ PAs	Armchair	77.358	-11.18	-7.46	0.175	-1.145	168.720	57.917
	Zigzag	77.358	7.12	-7.36	0.364	-1.038	145.690	47.812
AlGaN ₂	Armchair	201.19	-5.22	1.60	0.292	-0.899	1055.54	3649.21
	Zigzag	201.19	-5.16	1.50	0.305	-1.125	903.598	2898.91
AlGaP ₂	Armchair	102.065	-8.84	-6.56	0.122	-0.974	663.216	150.853
	Zigzag	102.065	-10.46	-6.58	0.122	-0.946	480.658	156.645
AlGaAs ₂	Armchair	85.863	-12.2	-7.36	0.098	-0.882	427.932	130.646
	Zigzag	89.297	-12.06	-7.32	0.098	-0.838	466.547	54.560
AlGaPAs	Armchair	84.814	-9.38	-6.27	0.108	-0.979	586.971	144.920
	Zigzag	88.349	-10.2	-7.56	0.107	-0.883	552.511	121.877
GaAlPAs	Armchair	95.714	-12.68	-8.44	0.104	-0.744	440.069	138.846
	Zigzag	95.714	-12.66	-8.42	0.104	-0.748	439.878	138.263

AlGaN₂ is quite small in both transport directions. Notably, AlGaN₂ also possesses a significant band gap (3.806 eV), which consequently signifies substantial potential applications in high-power and optoelectronic devices. Although the intrinsic carrier mobility of the other five structures may not be as outstanding as that of AlGaN₂, it remains comparable to well-known 2D monolayer materials, such as MoS₂ [57], Ga₂S₃ [47], Ga₂SSe₂ [26], and SnP₃ [28].

E. Photocatalytic water splitting properties of the MNXY monolayer

1. Optical properties and band-edge potential under different strains

To enable photocatalytic water splitting, a material must satisfy the following criteria [58]. (1) The band gap of the semiconductor material should be greater than the redox potential difference of water, which is 1.23 eV. (2) The edge potential should span the potentials of reducing H⁺/H₂ (-4.44 eV) and oxidizing O²/H₂O (-5.67 eV). (3) There should be a notable difference in the mobility of electrons and holes, facilitating efficient electron-hole separation. (4) The material should exhibit strong visible light absorption capabilities. Based on the previous state, materials with band gaps greater than 1.23 eV under the HSE06 functional include Al₂PAs, AlGaN₂, AlGaP₂, and GaAlPAs. Note that recent discovery has revealed that Janus materials exhibit a potential difference across their two ends because of the disruption of structural symmetry, leading to the presence of a dipole moment [59]. This characteristic enables materials with band gaps of less than 1.23 eV to exhibit highly efficient catalytic reactions. Regarding the electrostatic potential of the six structures in Fig. S7 of the Supplemental Material [40], all the structures except AlGaN₂ exhibit nearly identical potentials at both ends. Additionally, except for AlGaN₂, which has a dipole moment of 0.153 D, the remaining five structures have dipole moments smaller than 0.03 D, indicating their very limited magnitude. Hence, we disregard the impact of potential differences. Although AlGaN₂ possesses a band gap greater than 1.23 eV, its gap is relatively large (3.806 eV). We calculated the optical absorption coefficients of six different

structures under the HSE06 functional using the independent-electron approximation method [Fig. 6(a)]. This coefficient is calculated using the following formula [60]:

$$\alpha(\omega) = \sqrt{2} \frac{\omega}{c} \sqrt{\sqrt{\varepsilon_1(\omega)^2 + \varepsilon_2(\omega)^2} - \varepsilon_1(\omega)}, \quad (7)$$

where ω is the light frequency; c represents the speed of light; $\varepsilon_1(\omega)$ and $\varepsilon_2(\omega)$ are the real and imaginary parts of the dielectric function, respectively. AlGaN₂ exhibits almost no absorption peak in the visible light region. Thus its efficiency in absorbing visible light is limited. The intrinsic carrier mobility of Al₂PAs is relatively low, with a maximum value of only 168.72 cm² V⁻¹ S⁻¹. Likewise, it is also not suitable as a photocatalytic water splitting material. We need to focus solely on determining whether the band-edge potentials of AlGaP₂ and GaAlPAs meet the second condition mentioned above. The standard reduction potentials for H⁺/H₂ and O²/H₂O oxidation are given below [61]:

$$E_{\text{H}^+/\text{H}_2}^{\text{HER}} = -4.44 \text{ eV} + \text{pH} \times 0.059 \text{ eV}, \quad (8)$$

$$E_{\text{O}_2/\text{H}_2\text{O}}^{\text{OER}} = -5.67 \text{ eV} + \text{pH} \times 0.059 \text{ eV}, \quad (9)$$

herein, HER and OER stand for hydrogen evolution reaction and oxidation evolution reaction, respectively, when pH = 0, $E_{\text{H}^+/\text{H}_2}^{\text{HER}} = -4.44 \text{ eV}$, and $E_{\text{O}_2/\text{H}_2\text{O}}^{\text{OER}} = -5.67 \text{ eV}$. The strain-dependent band-edge potentials of AlGaP₂ and GaAlPAs are shown in Figs. 6(c) and 6(d). Strain can induce a transition from direct band gaps to indirect band gaps in both monolayer structures. Under no strain, AlGaP₂ spans the standard oxidation-reduction potential range, and even with applied compressive strain up to -4%, it remains within this range [Fig. 6(c)]. The optical absorption coefficients under compressive strain of 0% to -4% are shown in Fig. 6(b). The optical absorption coefficient of AlGaP₂ in the visible region is greater than 10⁴ cm⁻¹. As the compressive strain increases to -3%, the absorption peaks in the visible light region intensify and gradually undergo a blueshift. However, with a further increase in strain to -4%, the absorption peaks transitioned from the visible light region to the ultraviolet region. When subjected to biaxial tensile or compressive

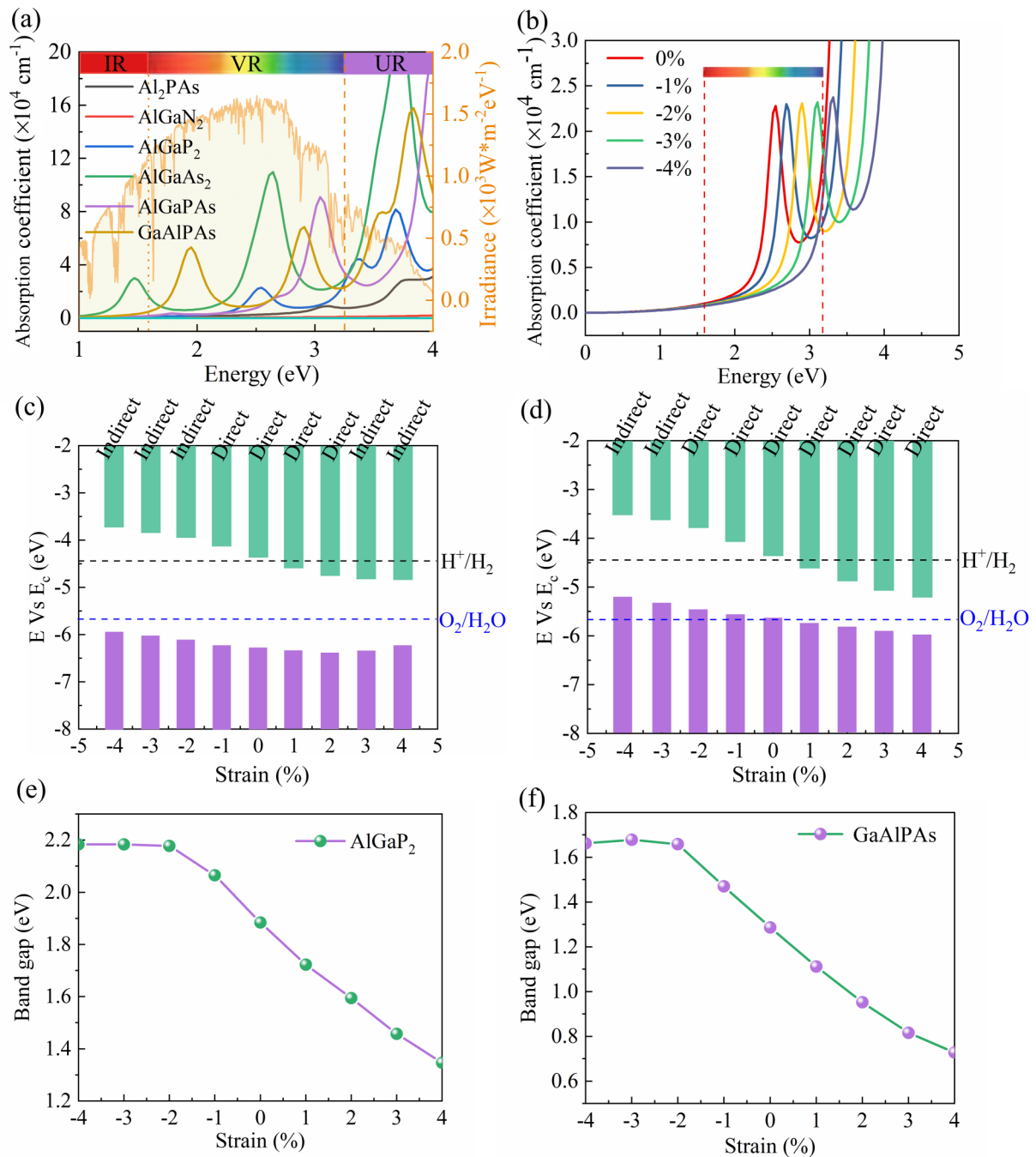


FIG. 6. (a) Absorption coefficients of six structures. (b) Variations in the absorption coefficients of AlGaP_2 under compressive strains ranging from 0% to -4%. Variation of the band-edge potential with respect to the redox potential under strains -4% to 4% and relationship between band gap and strain. (c), (e) AlGaP_2 , (d), (f) GaAlAs .

strain, GaAlPAs is unable to effectively span the standard oxidation-reduction potential range [Fig. 6(d)]; despite being similar to AlGaP_2 , the band gap gradually increases as the lattice constant decreases [Figs. 6(e) and 6(f)]. Therefore, AlGaP_2 emerges as a more promising candidate for photocatalytic materials, satisfying all the aforementioned criteria.

2. Solar to hydrogen (STH) efficiencies of AlGaP_2 monolayer

Improving the energy conversion efficiency of solar light is essential to achieving photocatalytic water splitting. We

consider the parameter known as the solar to hydrogen (η_{STH}) efficiency. To achieve meaningful large-scale applications, the η_{STH} value should exceed 10% [60]. We computed the light absorption efficiency η_{abs} , charge carrier utilization efficiency η_{cu} , and hydrogen production efficiency η_{STH} under different strains. These are evaluated using the following formulas, as outlined in previous research [62,63]:

$$\eta_{\text{abs}} = \frac{\int_{E_g}^{\infty} P(\hbar\omega)d(\hbar\omega)}{\int_0^{\infty} P(\hbar\omega)d(\hbar\omega)}, \quad (10)$$

$$\eta_{\text{cu}} = \frac{\Delta G \int_E^\infty \frac{P(\hbar\omega)}{\hbar\omega} d(\hbar\omega)}{\int_{E_g}^\infty P(\hbar\omega) d(\hbar\omega)}, \quad (11)$$

$$\eta_{\text{STH}} = \eta_{\text{abs}} \times \eta_{\text{cu}}. \quad (12)$$

Here, $P(\hbar\omega)$ represents the AM1.5G solar flux at the photon energy $\hbar\omega$, E_g represents the band gap of the monolayer, E represents the energy of photons that are effectively utilized for water splitting, and ΔG represents the oxidation-reduction potential difference of water at 1.23 eV. In Eq. (10), the

integral from 0 to ∞ in the denominator signifies the total power density of the AM1.5G. Meanwhile, the integral from E_g to ∞ in the numerator accounts for the power density that can be absorbed by the materials, while the integral from E to ∞ in the numerator represents the effective photocurrent density in Eq. (11). Taking into account the energy losses associated with charge carrier migration within the material, the assumed overpotentials for HER and OER are set at 0.2 and 0.6 eV, respectively. E is determined according to the following formula [59]:

$$E = \begin{cases} E_g, & [\chi(\text{H}_2) \geq 0.2, \chi(\text{O}_2) \geq 0.6] \\ E_g + 0.2 - \chi(\text{H}_2), & [\chi(\text{H}_2) < 0.2, \chi(\text{O}_2) \geq 0.6] \\ E_g + 0.6 - \chi(\text{O}_2), & [\chi(\text{H}_2) \geq 0.2, \chi(\text{O}_2) < 0.6] \\ E_g + 0.8 - \chi(\text{H}_2) - \chi(\text{O}_2), & [\chi(\text{H}_2) < 0.2, \chi(\text{O}_2) < 0.6] \end{cases} \quad (13)$$

Here, $\chi(\text{H}_2)$ and $\chi(\text{O}_2)$ represent the potential energy of the hydrogen and oxygen evolution reactions, respectively. The results of our calculations under varying strains are illustrated in Table IV. Notably, under no strain, η_{STH} reaches an impressive 17.51%, surpassing the previously reported values of GeN_3 (12.63%) [64], SiGeH_2 (13.22%) [65], $\text{AgBiP}_2\text{Se}_6$ (10.3%) [66], and InSe (12.59%) [59]. As compressive strain intensifies, the values of η_{abs} , η_{cu} , and η_{STH} decrease. With a strain of -4% , η_{STH} drops to 8.2%. However, under strain values ranging from 0% to -2% , η_{STH} remains consistently above 10%.

3. Changes in Gibbs free energy of HER and OER

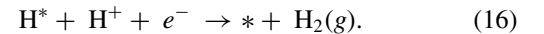
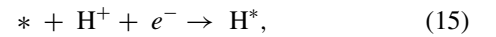
The determination of adsorption sites begins with the calculation of free energy. We have considered the adsorption energies of water molecules at five sites: the Al site, Ga site, P site, the center of the hexagon on the Al atomic plane (labeled H1), and center of the hexagon on the Ga atomic plane (labeled H2). Figure S8 of the Supplemental Material [40] illustrates the configuration diagrams of the adsorbed water molecules at different sites before and after structural optimization. Our results reveal that the structure of a H_2O molecule adsorbed on the H1 site is almost identical to that of the molecule adsorbed on the Al site after structural optimization. The adsorption energy of H2 is 2.82 eV, indicating an endothermic reaction and making spontaneous adsorption on the H2 site difficult. The adsorption energies for the Al, Ga, and P sites are shown in Fig. 7(a): Ga site (-0.018 eV) > P site (-0.066 eV) > Al site (-0.593 eV). Thus AlGaP_2

exhibits favorable conditions for the energetic adsorption of H_2O molecules; the Al site exhibits the lowest adsorption energy.

The feasibility of the thermodynamics of the HER and OER can be determined based on the changes in the Gibbs free energy for each reaction step, as illustrated in Fig. 7(b). The expression for calculating the Gibbs free energy is as follows [67]:

$$G = E + E_{\text{ZPE}} - TS, \quad (14)$$

where E represents the total adsorption energy of the system, E_{ZPE} represents the zero-point vibrational energy, and TS represents the entropy correction term. For the HER process in an aqueous solution, the chemical equation is as follows:



Here, “*” represents the adsorption site on the monolayer catalytic material. The reaction process involves the catalytic adsorption of H^+ on the catalyst to form an intermediate H^* , which reacts with $\text{H}^+ + e^-$ in water to form H_2 . This reaction step requires the photon energy absorbed by the material to be greater than the reduction potential of H^+ . In Fig. 7(c), under conditions without illumination ($U = 0$), the ΔG_{H^*} is 1.077 eV, indicating that the HER process cannot proceed spontaneously. However, when illumination is applied ($U = 1.23$ V), the ΔG_{H^*} for both steps becomes downhill, thereby enabling the reaction to proceed spontaneously.

TABLE IV. The values of $\chi(\text{H}_2)$, $\chi(\text{O}_2)$, light absorption efficiency η_{abs} , charge carrier utilization efficiency η_{cu} , and hydrogen production efficiency η_{STH} under compressive strains 0% to -4% .

Strain	$\chi(\text{H}_2)/\text{eV}$	$\chi(\text{O}_2)/\text{eV}$	$\eta_{\text{abs}} (\%)$	$\eta_{\text{cu}} (\%)$	$\eta_{\text{STH}} (\%)$
0	0.07	0.59	41.96	41.72	17.51
-1%	0.31	0.52	33.80	42.26	14.28
-2%	0.50	0.45	29.13	37.23	10.85
-3%	0.60	0.35	28.90	32.97	9.53
-4%	0.71	0.25	28.90	28.38	8.20

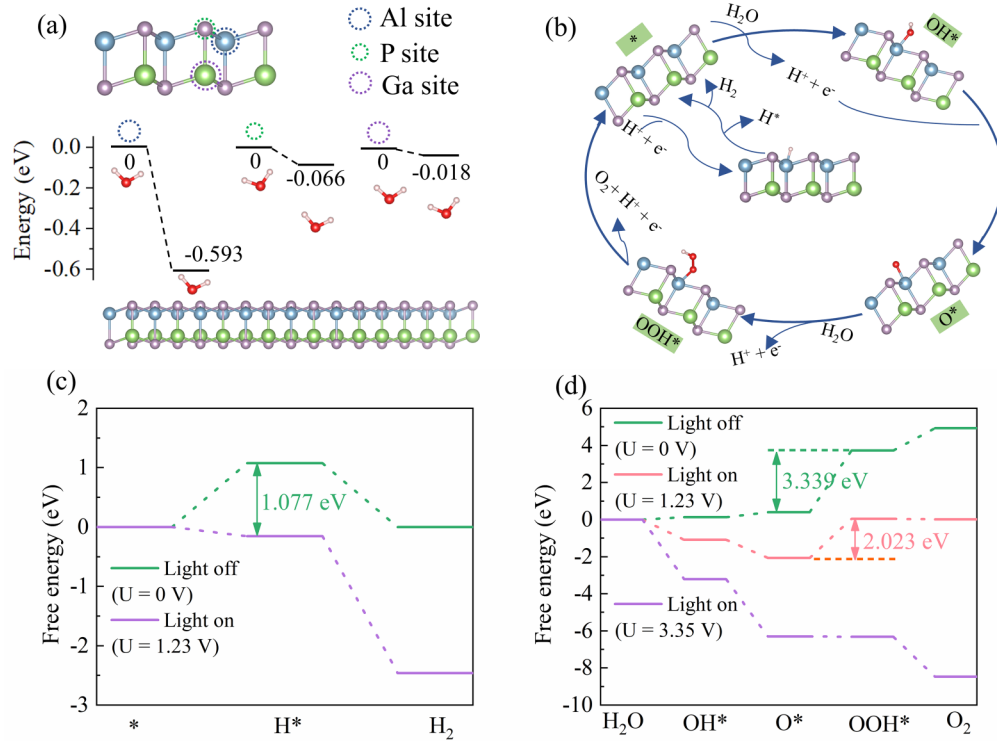
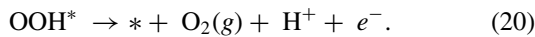
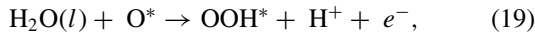
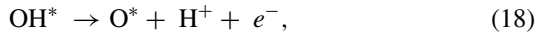
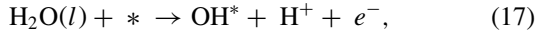


FIG. 7. (a) Adsorption energies of water molecules on different adsorption sites of the AlGaP₂ monolayer. (b) Mechanistic diagrams for each step of the chemical reactions in HER and OER. Variation of free energy for HER (c) and OER (d) at different voltages.

For the OER process, the steps are as follows:



Here, OH*, O*, and OOH* are the radicals involved in the reaction process. The catalyst * adsorbs water molecules, generating OH* and releasing a proton (H⁺) and an electron (e⁻) pair. Subsequently, OH* further dissociates to form O* while continuing to release H⁺ + e⁻. O* reacts with another water molecule on the catalyst, forming OOH*, eventually releasing a proton-electron pair to form O₂. The change in the Gibbs free energy for the OER process is shown in Fig. 7(d). Under dark conditions, the oxidation of O* to OOH* requires 3.339 eV. Upon illumination with an applied potential of $U = 1.23$ V, this energy requirement decreases to 2.023 eV. As U increases to 3.35 V, all Gibbs free energy values exhibit a descending trend. These results suggest that AlGaP₂ is an excellent photocatalytic material for water splitting.

IV. CONCLUSIONS

Herein, we conducted a screening of six monolayers with semiconducting properties from 15 novel MNXY monolayers using PBE generalization and verified the stability of these structures by phonon spectra, AIMD, and cohesive energy.

Despite the absence of imaginary frequencies in the phonon spectra of Al₂NP and AlGaNP, the AIMD simulations revealed structural instability. Subsequently, we investigated the mechanical properties of the six structures. AlGaNP exhibited the largest Young's modulus and Poisson's ratio of 169.889 N/m and 0.35, respectively. The remaining five displayed a Young's modulus of <90 N/m and a Poisson's ratio of <0.32. This not so large Young's modulus may allow for the stabilization of the MNXY monolayers with good strain capacity. The band gaps of the six monolayers were calculated from the electronic structures in the range of 0.846–3.806 eV. Furthermore, we calculated the intrinsic carrier mobility of the six structures. Thus we obtained that the mobility of holes in the armchair direction of AlGaNP is as high as 3649.21 cm² V⁻¹ s⁻¹, which exceeds that of electrons by 1055.54 cm² V⁻¹ s⁻¹. We also consider six monolayers for applications in the photocatalytic decomposition of water. Among the six monolayers, AlGaP₂ has a suitable band gap to span the band-edge potential of water, larger intrinsic carrier mobility, stronger light absorption, and a high hydrogen production efficiency of 17.51%. Additionally, it can maintain a hydrogen production efficiency of 10.85% with the enhancement of the intensity of light absorption at a compressive strain of -2%. The Gibbs free energy shows that the OER and HER processes can achieve superiority simultaneously under light conditions. Thus it is a candidate material for the efficient photocatalytic water splitting. These findings provide understanding for broadening the range of 2D semiconductor materials for preparing optoelectronic devices and selecting efficient catalysts.

ACKNOWLEDGMENTS

This paper was supported by the National Natural Science Foundation of China (Grants No. 52262021 and No. 51761004), the Industry and Education Combination Innovation Platform of Intelligent Manufacturing and Graduate Joint Training Base at Guizhou University (Grant No. 2020-

520000-83-01-324061), the Guizhou Province Science and Technology Fund, China (Grants No. ZK[2021]051 and No. ZK[2023]013), High-Level Creative Talent Training Program in Guizhou Province of China (Grant No. [2015]4015), and Guizhou Engineering Research Center for smart services (Grant No. 2203-520102-04-04-298868).

-
- [1] Y. Cao, V. Fatemi, S. Fang, K. Watanabe, T. Taniguchi, E. Kaxiras, and P. Jarillo-Herrero, Unconventional superconductivity in magic-angle graphene superlattices, *Nature (London)* **556**, 43 (2018).
- [2] F. Xia, H. Wang, J. C. Hwang, A. C. Neto, and L. Yang, Black phosphorus and its isoelectronic materials, *Nat. Rev. Phys.* **1**, 306 (2019).
- [3] S. Manzeli, D. Ovchinnikov, D. Pasquier, O. V. Yazyev, and A. Kis, 2D transition metal dichalcogenides, *Nat. Rev. Mater.* **2**, 1 (2017).
- [4] Y. Liu and T. Gao, First-principles study of controllable contact types in Janus MoSH/GaN van der Waals heterostructure, *J. Chem. Phys.* **159**, 091101 (2023).
- [5] A. Zavabeti, P. Aukarasereenont, H. Tuohey, N. Syed, A. Jannat, A. Elbourne, K. A. Messalea, B. Y. Zhang, B. J. Murdoch, and J. G. Partridge, High-mobility *p*-type semiconducting two-dimensional β -TeO₂, *Nat. Electron.* **4**, 277 (2021).
- [6] A. VahidMohammadi, J. Rosen, and Y. Gogotsi, The world of two-dimensional carbides and nitrides (MXenes), *Science* **372**, eabf1581 (2021).
- [7] H. Wang, Z. Li, D. Li, P. Chen, L. Pi, X. Zhou, and T. Zhai, Van der Waals integration based on two-dimensional materials for high-performance infrared photodetectors, *Adv. Funct. Mater.* **31**, 2103106 (2021).
- [8] M. Pollmann, H. H. Rotermund, G. Ertl, X. Li, and I. G. Kevrekidis, Formation of two-dimensional concentration pulses on microdesigned composite catalyst surfaces, *Phys. Rev. Lett.* **86**, 6038 (2001).
- [9] B. Wang, J. Iocozzia, M. Zhang, M. Ye, S. Yan, H. Jin, S. Wang, Z. Zou, and Z. Lin, The charge carrier dynamics, efficiency and stability of two-dimensional material-based perovskite solar cells, *Chem. Soc. Rev.* **48**, 4854 (2019).
- [10] Z. Kou, K. Wang, Z. Liu, L. Zeng, Z. Li, B. Yang, L. Lei, C. Yuan, and Y. Hou, Recent advances in manifold exfoliated synthesis of two-dimensional non-precious metal-based nanosheet electrocatalysts for water splitting, *Small Struct.* **3**, 2100153 (2022).
- [11] Y. Lin, Y. Li, Y. Cao, and X. Wang, Two-dimensional MOFs: Design & synthesis and applications, *Chem. Asian J.* **16**, 3281 (2021).
- [12] M. C. Lucking, W. Xie, D.-H. Choe, D. West, T.-M. Lu, and S. Zhang, Traditional semiconductors in the two-dimensional limit, *Phys. Rev. Lett.* **120**, 086101 (2018).
- [13] S. Dong and Y. Li, Excitonic instability and electronic properties of AlSb in the two-dimensional limit, *Phys. Rev. B* **104**, 085133 (2021).
- [14] L. Qin, Z.-H. Zhang, Z. Jiang, K. Fan, W.-H. Zhang, Q.-Y. Tang, H.-N. Xia, F. Meng, Q. Zhang, and L. Gu, Realization of AlSb in the double-layer honeycomb structure: A robust class of two-dimensional material, *ACS Nano* **15**, 8184 (2021).
- [15] B. Wan, Z. Gao, X. Huang, Y. Yang, L. Chen, Q. Wang, C. Fang, W. Shen, Y. Zhang, and H. Ma, Bonding heterogeneity inducing low lattice thermal conductivity and high thermoelectric performance in 2D CdTe₂, *ACS Appl. Energy Mater.* **5**, 9549 (2022).
- [16] S. Ahmed, A. Jalil, S. Z. Ilyas, H. Mufti, and S. Agathopoulos, The first-principles prediction of two-dimensional indium-arsenide bilayers, *Mater. Sci. Semicond. Process.* **134**, 106041 (2021).
- [17] K. Mustonen, C. Hofer, P. Kotrusz, A. Markevich, M. Hulman, C. Mangler, T. Susi, T. J. Pennycook, K. Hricovini, and C. Richter, Toward exotic layered materials: 2D cuprous iodide, *Adv. Mater.* **34**, 2106922 (2022).
- [18] B. Andryushechkin and T. Pavlova, Adsorption of molecular iodine on the Ag (111) surface: Phase transitions, silver reconstruction, and iodide growth, *J. Chem. Phys.* **156**, 164702 (2022).
- [19] D. Kitchen, A. Richardella, J.-M. Tang, M. E. Flatté, and A. Yazdani, Atom-by-atom substitution of Mn in GaAs and visualization of their hole-mediated interactions, *Nature (London)* **442**, 436 (2006).
- [20] H. Li, H. Liu, L. Zhou, X. Wu, Y. Pan, W. Ji, B. Zheng, Q. Zhang, X. Zhuang, and X. Zhu, Strain-tuning atomic substitution in two-dimensional atomic crystals, *ACS Nano* **12**, 4853 (2018).
- [21] R. Li, S. Pang, C. Ma, and T. Zhang, Influence of similar atom substitution on glass formation in (La–Ce)–Al–Co bulk metallic glasses, *Acta Mater.* **55**, 3719 (2007).
- [22] Y. Mao, P. Wang, L. Li, Z. Chen, H. Wang, Y. Li, and S. Zhan, Unravelling the synergy between oxygen vacancies and oxygen substitution in BiO_{2-x} for efficient molecular-oxygen activation, *Angew. Chem. Int. Ed.* **59**, 3685 (2020).
- [23] A.-Y. Lu, H. Zhu, J. Xiao, C.-P. Chuu, Y. Han, M.-H. Chiu, C.-C. Cheng, C.-W. Yang, K.-H. Wei, and Y. Yang, Janus monolayers of transition metal dichalcogenides, *Nat. Nanotechnol.* **12**, 744 (2017).
- [24] Y. Zheng, X. Tang, W. Wang, L. Jin, and G. Li, Large-size ultrathin α -Ga₂S₃ nanosheets toward high-performance photodetection, *Adv. Funct. Mater.* **31**, 2008307 (2021).
- [25] H. Liu, K. A. Antwi, N. Yakovlev, H. Tan, L. Ong, S. Chua, and D. Chi, Synthesis and phase evolutions in layered structure of Ga₂S₃ semiconductor thin films on epitaxially grown GaAs (111) substrates, *ACS Appl. Mater. Interfaces* **6**, 3501 (2014).
- [26] N. N. Hieu, H. V. Phuc, A. Kartamyshev, and T. V. Vu, Structural, electronic, and transport properties of quintuple atomic Janus monolayers Ga₂SX₂ (X = O, S, Se, Te): First-principles predictions, *Phys. Rev. B* **105**, 075402 (2022).
- [27] C. Qi, C. Yan, Q. Li, T. Yang, S. Qiu, and J. Cai, Two-dimensional Janus monolayers Al₂XYZ (X/Y/Z = S, Se, Te, X ≠ Y ≠ Z): First-principles insight into the photocatalytic and

- highly adjustable piezoelectric properties, *J. Mater. Chem. C* **11**, 3262 (2023).
- [28] S. Sun, F. Meng, H. Wang, H. Wang, and Y. Ni, Novel two-dimensional semiconductor SnP₃: High stability, tunable bandgaps and high carrier mobility explored using first-principles calculations, *J. Mater. Chem. A* **6**, 11890 (2018).
- [29] Y.-L. Liu, X.-X. Jiang, B. Li, Y. Shi, D.-S. Liu, and C.-L. Yang, First principles study of photoelectrochemical water splitting in monolayer Sn₂S₂P₄ with high solar-to-hydrogen efficiency, *Appl. Phys. Lett.* **119**, 143102 (2021).
- [30] W. Shi, K. Fan, and Z. Wang, Catalytic activity for the hydrogen evolution reaction of edges in Janus monolayer MoXY (*XY* = S, Se, and Te), *Phys. Chem. Chem. Phys.* **20**, 29423 (2018).
- [31] G. Kresse and J. Furthmüller, Efficient iterative schemes for *ab initio* total-energy calculations using a plane-wave basis set, *Phys. Rev. B* **54**, 11169 (1996).
- [32] G. Kresse and J. Hafner, *Ab initio* molecular dynamics for open-shell transition metals, *Phys. Rev. B* **48**, 13115 (1993).
- [33] M. Ernzerhof and G. E. Scuseria, Assessment of the Perdew–Burke–Ernzerhof exchange–correlation functional, *J. Chem. Phys.* **110**, 5029 (1999).
- [34] J. Heyd, G. E. Scuseria, and M. Ernzerhof, Hybrid functionals based on a screened Coulomb potential, *J. Chem. Phys.* **118**, 8207 (2003).
- [35] J. P. Perdew, M. Ernzerhof, and K. Burke, Rationale for mixing exact exchange with density functional approximations, *J. Chem. Phys.* **105**, 9982 (1996).
- [36] S. Grimme, S. Ehrlich, and L. Goerigk, Effect of the damping function in dispersion corrected density functional theory, *J. Comput. Chem.* **32**, 1456 (2011).
- [37] T. Sohler, M. Calandra, and F. Mauri, Density functional perturbation theory for gated two-dimensional heterostructures: Theoretical developments and application to flexural phonons in graphene, *Phys. Rev. B* **96**, 075448 (2017).
- [38] P. Giannozzi, S. De Gironcoli, P. Pavone, and S. Baroni, *Ab initio* calculation of phonon dispersions in semiconductors, *Phys. Rev. B* **43**, 7231 (1991).
- [39] M. Faraji, A. Bafekry, M. M. Fadlallah, H. Jappor, C. V. Nguyen, and M. Ghergherehchi, Two-dimensional XY monolayers (*X* = Al, Ga, In; *Y* = N, P, As) with a double layer hexagonal structure: A first-principles perspective, *Appl. Surf. Sci.* **590**, 152998 (2022).
- [40] See Supplemental Material at <http://link.aps.org/supplemental/10.1103/PhysRevB.108.245424> for the atomic configurations of the 15 MNXY monolayer structures after optimization; the band structures of the 15 different MNXY monolayer structures; structural variation plots for eight monolayers running AIMD at 300 K after 8 ps; stress-strain and energy change curves of Al₂PAs under biaxial tensile and compressive strains; ELF plots for the six structural unit cells; electrostatic potentials of six structures under the HSE06 function; and before and after optimization of the molecular structure of H₂O adsorbed at five adsorption sites.
- [41] H. Watanabe and S. Takagi, Effects of incomplete ionization of impurities in poly-Si gate and band gap narrowing on direct tunneling gate leakage current, *J. Appl. Phys.* **90**, 1600 (2001).
- [42] M. Yamada, Y. Yamakita, and K. Ohno, Phonon dispersions of hydrogenated and dehydrogenated carbon nanoribbons, *Phys. Rev. B* **77**, 054302 (2008).
- [43] T. Sohler, M. Gibertini, M. Calandra, F. Mauri, and N. Marzari, Breakdown of optical phonons’ splitting in two-dimensional materials, *Nano Lett.* **17**, 3758 (2017).
- [44] M. Mihalkovič and M. Widom, First-principles calculations of cohesive energies in the Al–Co binary alloy system, *Phys. Rev. B* **75**, 014207 (2007).
- [45] J. Guan, Z. Zhu, and D. Tománek, Phase coexistence and metal-insulator transition in few-layer phosphorene: A computational study, *Phys. Rev. Lett.* **113**, 046804 (2014).
- [46] X. Lin and J. Ni, Much stronger binding of metal adatoms to silicene than to graphene: A first-principles study, *Phys. Rev. B* **86**, 075440 (2012).
- [47] G. Zhang, K. Lu, Y. Wang, H. Wang, and Q. Chen, Mechanical and electronic properties of α -M₂X₃ (*M* = Ga, In; *X* = S, Se) monolayers, *Phys. Rev. B* **105**, 235303 (2022).
- [48] E. Cadelano, P. L. Palla, S. Giordano, and L. Colombo, Elastic properties of hydrogenated graphene, *Phys. Rev. B* **82**, 235414 (2010).
- [49] J. M. Carlsson and M. Scheffler, Structural, electronic, and chemical properties of nanoporous carbon, *Phys. Rev. Lett.* **96**, 046806 (2006).
- [50] M. Topsakal, E. Aktürk, and S. Ciraci, First-principles study of two- and one-dimensional honeycomb structures of boron nitride, *Phys. Rev. B* **79**, 115442 (2009).
- [51] R. C. Cooper, C. Lee, C. A. Marianetti, X. Wei, J. Hone, and J. W. Kysar, Nonlinear elastic behavior of two-dimensional molybdenum disulfide, *Phys. Rev. B* **87**, 035423 (2013).
- [52] A. D. Becke and K. E. Edgecombe, A simple measure of electron localization in atomic and molecular systems, *J. Chem. Phys.* **92**, 5397 (1990).
- [53] P. A. Schultz, Theory of defect levels and the “band gap problem” in silicon, *Phys. Rev. Lett.* **96**, 246401 (2006).
- [54] Z. Y. Al Balushi, K. Wang, R. K. Ghosh, R. A. Vilá, S. M. Eichfeld, J. D. Caldwell, X. Qin, Y.-C. Lin, P. A. DeSario, and G. Stone, Two-dimensional gallium nitride realized via graphene encapsulation, *Nat. Mater.* **15**, 1166 (2016).
- [55] P. Erhart, A. Klein, R. G. Egdell, and K. Albe, Band structure of indium oxide: Indirect versus direct band gap, *Phys. Rev. B* **75**, 153205 (2007).
- [56] J. Bardeen and W. Shockley, Deformation potentials and mobilities in non-polar crystals, *Phys. Rev.* **80**, 72 (1950).
- [57] B. Radisavljevic, A. Radenovic, J. Brivio, V. Giacometti, and A. Kis, Single-layer MoS₂ transistors, *Nat. Nanotechnol.* **6**, 147 (2011).
- [58] H. Guo, Z. Zhang, B. Huang, X. Wang, H. Niu, Y. Guo, B. Li, R. Zheng, and H. Wu, Theoretical study on the photocatalytic properties of 2D InX (*X* = S, Se)/transition metal disulfide (MoS₂ and WS₂) van der Waals heterostructures, *Nanoscale* **12**, 20025 (2020).
- [59] C.-F. Fu, J. Sun, Q. Luo, X. Li, W. Hu, and J. Yang, Intrinsic electric fields in two-dimensional materials boost the solar-to-hydrogen efficiency for photocatalytic water splitting, *Nano Lett.* **18**, 6312 (2018).
- [60] M. Fox and G. F. Bertsch, Optical properties of solids, *Am. J. Phys.* **70**, 1269 (2002).
- [61] G. L. Qian, Q. Xie, Q. Liang, X. Y. Luo, and Y. X. Wang, Electronic properties and photocatalytic water splitting with high solar-to-hydrogen efficiency in a hBNC/Janus WSSe heterojunction: First-principles calculations, *Phys. Rev. B* **107**, 155306 (2023).

- [62] Z. Chen, T. F. Jaramillo, T. G. Deutsch, A. Kleiman-Shwarscstein, A. J. Forman, N. Gaillard, R. Garland, K. Takanabe, C. Heske, and M. Sunkara, Accelerating materials development for photoelectrochemical hydrogen production: Standards for methods, definitions, and reporting protocols, *J. Mater. Res.* **25**, 3 (2010).
- [63] L.-B. Zhan, C.-L. Yang, M.-S. Wang, and X.-G. Ma, Discovery of two-dimensional Ga₂S₃ monolayers for efficient photocatalytic overall water splitting to produce hydrogen, *Appl. Surf. Sci.* **626**, 157215 (2023).
- [64] J. Liu, Y. Shen, X. Gao, L. Lv, Y. Ma, S. Wu, X. Wang, and Z. Zhou, GeN₃ monolayer: A promising 2D high-efficiency photo-hydrolytic catalyst with high carrier mobility transport anisotropy, *Appl. Catal., B* **279**, 119368 (2020).
- [65] Q. Li, H.-Y. Liu, H. Yang, and Y. Zheng, High carrier mobilities and tunable band structures in two-dimensional MNH₂ ($M, N = \text{C, Si, Ge}$) monolayers, *Appl. Surf. Sci.* **615**, 156197 (2023).
- [66] L. Ju, J. Shang, X. Tang, and L. Kou, Tunable photocatalytic water splitting by the ferroelectric switch in a 2D AgBiP₂Se₆ monolayer, *J. Am. Chem. Soc.* **142**, 1492 (2019).
- [67] W. Zhang, S. Xi, Y. Liang, and C. He, Construction of novel PG/GeP₂ and PG/SiP₂ vdW heterostructures for high-efficiency photocatalytic water splitting, *Appl. Surf. Sci.* **608**, 155106 (2023).